

# Strong Limit on a Variable Proton-to-Electron Mass Ratio from Molecules in the Distant Universe

Michael T. Murphy,<sup>1\*</sup> Victor V. Flambaum,<sup>2</sup> Sébastien Muller,<sup>3</sup>  
Christian Henkel<sup>4</sup>

<sup>1</sup>Centre for Astrophysics and Supercomputing, Swinburne University of Technology,  
Mail H39, PO Box 218, Victoria 3122, Australia

<sup>2</sup>School of Physics, University of New South Wales, Sydney, N.S.W. 2052, Australia

<sup>3</sup>Academia Sinica Institute of Astronomy and Astrophysics,  
PO Box 23-141, Taipei, 106 Taiwan

<sup>4</sup>Max-Planck-Institut für Radioastronomie, Auf dem Hügel 69, 53121 Bonn, Germany

\*To whom correspondence should be addressed; E-mail: mmurphy@swin.edu.au.

**The Standard Model of particle physics assumes that the so-called fundamental constants are universal and unchanging. Absorption lines arising in molecular clouds along quasar sightlines offer a precise test for variations in the proton-to-electron mass ratio,  $\mu$ , over cosmological time and distance scales. The inversion transitions of ammonia are particularly sensitive to  $\mu$  compared to molecular rotational transitions. Comparing the available ammonia spectra observed towards the quasar B0218+357 with new, high-quality rotational spectra, we present the first detailed measurement of  $\mu$  with this technique, limiting relative deviations from the laboratory value to  $|\Delta\mu/\mu| < 1.8 \times 10^{-6}$  (95% confidence level) at approximately half the Universe's current age – the strongest astrophysical constraint to date. Higher-quality ammonia observations will reduce both the statistical and systematic uncertainties in these measurements.**

The Standard Model of particle physics assumes that the fundamental constants of nature (or, at least, their low-energy limits) are the same everywhere and at every epoch in the Universe. However, it cannot itself justify this assumption, nor can it predict their values. Our confidence in their constancy stems from Earth-bound laboratory experiments conducted over

human time-scales. Extrapolating to the entire Universe seems unwise, especially considering that the physics driving the Universe’s accelerating expansion, labeled ‘Dark Energy’, is completely unknown. Nevertheless, the Earth-bound experiments achieve impressive precision: time-variations in the fine-structure constant,  $\alpha \equiv e^2/\hbar c$ , which measures the strength of electromagnetism, are limited to  $\dot{\alpha}/\alpha = (-1.6 \pm 2.3) \times 10^{-17} \text{ yr}^{-1}$ , while those in the proton-to-electron mass ratio,  $\mu \equiv m_p/m_e$  – effectively the ratio of the strong and electro-weak scales – are limited to  $\dot{\mu}/\mu = (-1.9 \pm 4.0) \times 10^{-16} \text{ yr}^{-1}$  (1). Still, more dramatic variations might have occurred over the 13–14 Gyr history of the Universe and the residual variations in our small space-time region might remain undetectably small. It is therefore imperative to measure the constants over cosmological time- and distance-scales.

Variations in  $\mu$  and/or  $\alpha$  would manifest themselves as shifts in the transition energies of atoms and molecules. By comparing transition energies registered in spectra of astronomical objects with laboratory values, possible variations can, in principle, be probed over our entire observable Universe and through most of its history. Due to the narrowness of the spectral features involved, absorption lines arising in gas clouds along lines of sight to background quasars are currently our most precise cosmological probes. For example, by comparing various heavy element electromagnetic resonance transitions in optical quasar spectra, 5- $\sigma$  evidence has emerged for variations in  $\alpha$  of  $\sim 5$  parts in  $10^6$  at redshifts  $0.2 < z < 4.2$  (2, 3, 4, 5). Although a more recent statistical sample found no variation (6), errors in the analysis prevent reliable interpretation of those results (7, 8), leaving open the possibility of a varying  $\alpha$ .

Similarly, tentative (3- $\sigma$ ) evidence for a fractional variation in  $\mu$  of  $\sim 20 \times 10^{-6}$  has recently come from 2 quasar spectra containing many ultraviolet (UV)  $\text{H}_2$  transitions at redshift  $z \sim 2.8$  (9, 10). Comparison of UV heavy-element resonance lines and H I 21-cm absorption is sensitive to  $\alpha^2\mu$  and, assuming  $\alpha$  to be constant, has yielded indirect null constraints on  $\mu$ -variation, albeit with slightly worse precision than the direct  $\text{H}_2$  method (11).

An alternative method for measuring  $\mu$  at high redshift, suggested recently by Flambaum & Kozlov (12), is to utilize the sensitivity to  $\mu$ -variation of the ammonia inversion transitions (13) near 24 GHz. A shift in their frequencies due to a varying  $\mu$  can be discerned from the cosmological redshift by comparing them to transitions with lower sensitivity to  $\mu$ . Good candidates for comparison are rotational transitions of molecules such as CO,  $\text{HCO}^+$  and HCN because (i) their transition frequencies depend mainly on  $\mu$  and not on other fundamental quantities (e.g.  $\alpha$ ); (ii) they are simple molecules, commonly detected in the interstellar medium; (iii) their rest frequencies (80–200 GHz) are not vastly dissimilar to the  $\text{NH}_3$  transitions’ (cf. comparison of UV and 21-cm), thus reducing possible effects due to frequency-dependent spatial structure in the background quasar’s emission. This final point is discussed in more detail below.

For rotational and  $\text{NH}_3$  inversion transitions we may write the apparent change in velocity or redshift of an absorption line due to a variation in  $\mu$  as

$$\frac{\Delta v}{c} = \frac{\Delta z}{1+z} = K_i \frac{\Delta \mu}{\mu}, \quad (1)$$

where  $K_i$  is the sensitivity of transition  $i$  to  $\mu$  and  $\Delta\mu/\mu \equiv (\mu_z - \mu_{\text{lab}})/\mu_{\text{lab}}$  for  $\mu_{\text{lab}}$  and  $\mu_z$

the values of  $\mu$  in the laboratory and absorption cloud at redshift  $z$ , respectively. All rotational transitions have  $K_i = 1$ , so comparing them with each other provides no constraint on  $\Delta\mu/\mu$ . However, the sensitivity of the  $\text{NH}_3$  inversion transitions is strongly enhanced,  $K_i \approx 4.46$  (12). That is, as  $\mu$  varies the  $\text{NH}_3$  transitions shift relative to the rotational transitions.

Only one quasar absorption system displaying  $\text{NH}_3$  absorption is currently known, that at  $z = 0.68466$  towards quasar B0218+357. From redshift uncertainty estimates for  $\text{NH}_3$ , CO,  $\text{HCO}^+$  and HCN in the literature, (12) crudely estimated the precision achievable to be  $\delta(\Delta\mu/\mu) \approx 2 \times 10^{-6}$ . However, (12) cautioned that a proper measurement of  $\Delta\mu/\mu$  from  $\text{NH}_3$  would require detailed, simultaneous fits to all the molecular transitions and that significantly better precision may be possible. Here we make the first detailed measurement of  $\mu$  using the  $\text{NH}_3$  inversion transitions by comparison with  $\text{HCO}^+$  and HCN rotational transitions.

The only published  $\text{NH}_3$  absorption spectra are those for the  $(J,K) = (1,1)$ ,  $(2,2)$  and  $(3,3)$  inversion transitions reported by (14) towards B0218+357, reproduced in Fig. 1. The channel spacing is  $1.67 \text{ km s}^{-1}$  for  $(1,1)$  &  $(2,2)$  and  $3.3 \text{ km s}^{-1}$  for  $(3,3)$ . The spectra are normalized by a low-order fit to the quasar continuum. See (14) for observational and data reduction details. The signal-to-noise ratio (SNR) for the flux is very high,  $\sim 1000$  per channel, but since  $< 1\%$  of the continuum is absorbed, the effective SNR for the optical depth is quite low.

$\text{HCO}^+$  and  $\text{HCN}(1-2)$  absorption towards B0218+357 was discovered more than a decade ago (15). New, high resolution ( $\approx 0.9 \text{ km s}^{-1}$  per channel), high SNR ( $\sim 100$  per channel) observations of these lines were recently undertaken with the Plateau de Bure Interferometer, France; see (16). Fig. 1 shows both spectra normalized by fits to the quasar continuum.

All spectra were registered to the heliocentric reference frame; possible errors in this procedure are discussed in (16) and shown to be negligible.

Spectra representing the  $1-\sigma$  uncertainty in normalized flux per channel were constructed for all the molecular spectra by calculating the root-mean-square (RMS) flux variations in the continuum portions of each transition. Since no large differences were observed either side of the absorption for any transition, a simple constant error model was adopted.

As equation 1 states, the signature of a varying  $\mu$  would be a velocity shift between the rotational and  $\text{NH}_3$  inversion transitions. Complicating the measurement of any shift is the ‘velocity structure’ evident in Fig. 1: the profiles comprise absorption from many gas clouds, all associated with the absorbing galaxy but nevertheless moving at different velocities. The number and velocity distribution of these ‘velocity components’ are unknown and must be determined from the data themselves. Each fitted velocity component is represented by a Gaussian profile parametrized by its optical depth, Doppler width and redshift. The best-fitting parameter values are determined with a  $\chi^2$ -minimization code, VPFIT (17), designed specifically for fitting quasar absorption lines. To determine the statistically preferred velocity structure, the best fit (i.e. minimized) values of  $\chi^2$  per degree of freedom,  $\chi_\nu^2$ , are compared for several fits with different velocity structures. That with the lowest  $\chi_\nu^2$  is taken as the fiducial one (i.e. an F-test to discriminate between models).

Measuring  $\Delta\mu/\mu$  requires the assumption that the velocity structure is the same in all transitions. This does *not* mean that the ratio of optical depths of corresponding velocity components

in different transitions must be constant across the profile. Rather, it means that the number and velocity distribution of components are assumed to be the same in different transitions. We discuss this assumption below but, since it must be made eventually, in practice the velocity structure was determined by tying together the redshifts of corresponding velocity components in different transitions. The high SNR rotational spectra clearly place the strongest constraints on the velocity structure but the  $\text{NH}_3$  spectra must be included to measure  $\Delta\mu/\mu$ . The Doppler widths of corresponding components were also tied together, effectively assuming a turbulent broadening mechanism.

Figure 1 shows the fiducial 8-component fit. Note that the detailed hyperfine structure of the  $\text{HCN}(1-2)$  and  $\text{NH}_3$  transitions is reflected in each velocity component. The relative hyperfine level populations were fixed by assuming local thermodynamic equilibrium (LTE). The laboratory data used in the fits are tabulated in (16). Given this fit, determining  $\Delta\mu/\mu$  is straightforward: a single additional free parameter is introduced for the entire absorption system which shifts all the velocity components of each transition according to its  $K$ -coefficient (equation 1). All parameters in the fit, including the single value of  $\Delta\mu/\mu$ , are varied by VPFIT to minimize  $\chi^2$ . The best-fit value is  $\Delta\mu/\mu = (+0.74 \pm 0.47) \times 10^{-6}$ , corresponding to a (statistically insignificant) velocity shift between the  $\text{NH}_3$  and rotational transitions of  $0.77 \pm 0.49 \text{ km s}^{-1}$ . The  $1-\sigma$  error quoted here – formed from the diagonal terms of the final parameter covariance matrix – derives entirely from the photon statistics of the absorption spectra. A different (though intimately related) approach to determining  $\Delta\mu/\mu$  and its error is discussed in (16); it provides the same result.

Fitting too few velocity components causes large systematic errors in such analyses (8). A reliable measurement of  $\Delta\mu/\mu$  can only be derived from fits replicating all the statistically significant structure in the absorption profiles. Therefore, the fiducial velocity structure must be the statistically preferred one. When fitting many transitions simultaneously, this may be more complicated than the one preferred by human eye. The simplest objective method to achieve this is demonstrated in Fig. 2 which shows the decrease in  $\chi^2$  as increasingly complex velocity structures are fitted. When the fit is too simple to adequately describe the data, quite different values of  $\Delta\mu/\mu$  are found. On the other hand, the 9-component ‘over-fitted’ case provides a value and error very similar to the fiducial 8-component model.

The consistency of the velocity structures in the two highest SNR transitions,  $\text{HCO}^+$  and  $\text{HCN}(1-2)$ , was tested by fitting those transitions independently. Again, different fits with different velocity structures were compared to determine the statistically preferred one. Both transitions are best fit by velocity structures similar to that in Fig. 1 [see (16)], providing some confidence that they can meaningfully be fitted simultaneously. These independent velocity structures were applied to the  $\text{NH}_3$  transitions and new values of  $\Delta\mu/\mu$  derived. When fitting only  $\text{HCO}^+(1-2)$  and  $\text{NH}_3$ ,  $\Delta\mu/\mu = (+0.67 \pm 0.51) \times 10^{-6}$ ; for  $\text{HCN}(1-2)$  and  $\text{NH}_3$ ,  $\Delta\mu/\mu = (+0.88 \pm 0.51) \times 10^{-6}$ . Neither value substantially deviates from our fiducial one. Note that the marginal increase in the  $1-\sigma$  error when using a single rotational transition indicates that the  $\text{NH}_3$  spectra limit the statistical uncertainty.

To consider potential systematic uncertainties, it is important to recall our main assumption:

the velocity components constituting the absorption profiles have the same redshifts in different transitions. While the  $\text{HCO}^+$  and  $\text{HCN}(1-2)$  velocity structures are evidently similar enough for measuring  $\Delta\mu/\mu$ , the  $\text{NH}_3$  spectra have too low SNR for a direct comparison. And since the observed frequencies of the  $\text{NH}_3$  ( $\sim 14$  GHz) and rotational ( $\sim 106$  GHz) transitions are somewhat different, it is possible that, if the background source morphology is frequency dependent, some  $\text{NH}_3$  components might arise along slightly different sight-lines to those components in the rotational profiles. This is considered presently.

B0218+357 is a  $z = 0.944$  BL Lac object (18) lensed by a nearly face-on Sa/Sab  $z = 0.68$  galaxy (19) in which the absorption occurs. Two lensed images, A and B, separated by 334 mas, straddle the lensing galaxy’s center with image B much closer to the center. An Einstein ring with diameter  $\sim 300$  mas, centered near image B, has also been identified (20). B0218+357 itself has a core–jet morphology with an unresolved [ $< 1 \times 1$  mas or  $< 7 \times 7$  pc (21)] flat-spectrum core dominating the observed 8.4 GHz emission (22). The jet has a knotty structure extending over  $\sim 10 \times 10$  mas and, like other jets, is expected to have a steep spectrum.

Various absorption lines have been detected in the  $z = 0.68466$  absorber, from HI 21-cm and OH below (rest-frame) 2 GHz (23, 24), through six  $\text{H}_2\text{CO}$  transitions at 5–150 GHz (25), to  $\text{H}_2\text{O}$  at 557 GHz (26) to name but a few. Furthermore, the molecular absorption arises only towards image A (27, 28, 29, 25). The flat-spectrum core should completely dominate at high frequencies; that  $\text{H}_2\text{CO}$  and  $\text{H}_2\text{O}$  absorb most of the total high-frequency continuum therefore implies that at least those transitions only arise towards the core. All the observed molecular transitions have consistent velocity structures (though most spectra have poorer resolution and/or SNR than those studied here). Thus, the most important velocity components in all transitions evidently arise towards image A’s flat-spectrum, compact core (14, 29).

Nevertheless, indirect evidence suggests that the molecular clouds do not completely cover the background source (30, 16). If the covering fraction is different for the rotational and  $\text{NH}_3$  transitions, some velocity components may appear in one and not the other. Similar problems may arise because some  $\text{HCO}^+$  and  $\text{HCN}(1-2)$  velocity components may be optically thick (16). The spurious shifts in  $\Delta\mu/\mu$  these effects may cause are difficult to estimate in general but in (16) we conduct several fits in which different combinations of  $\text{NH}_3$  velocity components are removed, providing an estimate of  $\pm 0.7 \times 10^{-6}$ . Another potential systematic error is our assumption of LTE for the  $\text{HCN}(1-2)$  and  $\text{NH}_3$  hyperfine structure populations. As mentioned above, removing  $\text{HCN}(1-2)$  from the analysis barely changes the measured  $\Delta\mu/\mu$ . Removing different parts of the hyperfine structure from the  $\text{NH}_3$  transitions results in maximum deviations of  $\pm 0.3 \times 10^{-6}$  from our fiducial value of  $\Delta\mu/\mu$  (16).

Combining these two potential systematic errors in quadrature, we obtain  $\Delta\mu/\mu = (+0.74 \pm 0.47_{\text{stat}} \pm 0.76_{\text{sys}}) \times 10^{-6}$ , providing no evidence for cosmological variations in  $\mu$ . The  $\text{NH}_3$  spectra currently set both the statistical and systematic errors. While, clearly, the SNR and resolution directly determine the former, they also indirectly influence the latter: the velocity structure of higher quality  $\text{NH}_3$  spectra could be more directly compared with the rotational profiles and limits on non-LTE hyperfine structure anomalies could be constrained by the data themselves. That is, with improved  $\text{NH}_3$  spectra, both the statistical and systematic error com-

ponents can be improved. Nevertheless, until the  $\text{NH}_3$  data are improved, our final result is a  $2\text{-}\sigma$  limit on variation in  $\mu$  from this single absorber:  $|\Delta\mu/\mu| < 1.8 \times 10^{-6}$ . This corresponds to  $< 1.9 \text{ km s}^{-1}$  shift between the  $\text{NH}_3$  and rotational transitions.

Our new value of  $\Delta\mu/\mu$  seems inconsistent with the current tentative evidence for  $\mu$ -variation from  $\text{H}_2$  absorption at  $z \sim 2.8$ ,  $\Delta\mu/\mu = (+24.4 \pm 5.9) \times 10^{-6}$  (10). However, reliable comparison is difficult because cosmological time- and/or space-variations in  $\mu$  remain poorly constrained. Clearly, a statistical sample from both techniques, covering a wide redshift range and with detailed assessment of systematic effects, is highly desirable.

Assuming  $\mu$  varies linearly with time, our measurement corresponds to a drift of  $\dot{\mu}/\mu = (-1.2 \pm 0.8_{\text{stat}} \pm 1.2_{\text{sys}}) \times 10^{-16} \text{ yr}^{-1}$ . However, this assumption is only a convenient means for comparison with current limits from laboratory atomic clocks,  $\dot{\mu}/\mu = (-1.9 \pm 4.0) \times 10^{-16} \text{ yr}^{-1}$  (1); it is not motivated by any physical (necessarily untested) varying- $\mu$  theory.

With so few measurements of  $\mu$  distributed throughout the Universe, each new measurement is an invaluable test of the most basic – and theoretically unjustifiable – assumptions in the Standard Model: that the laws of physics are universal and unchanging. The precision demonstrated here highlights the importance of discovering many more molecular absorbers to our knowledge of fundamental physics.

## References and Notes

1. T. Rosenband, *et al.*, *Science* **319**, 1808 (2008).
2. J. K. Webb, V. V. Flambaum, C. W. Churchill, M. J. Drinkwater, J. D. Barrow, *Phys. Rev. Lett.* **82**, 884 (1999).
3. M. T. Murphy, *et al.*, *Mon. Not. Roy. Astron. Soc.* **327**, 1208 (2001).
4. M. T. Murphy, J. K. Webb, V. V. Flambaum, *Mon. Not. Roy. Astron. Soc.* **345**, 609 (2003).
5. M. T. Murphy, *et al.*, *Lecture Notes Phys.* **648**, 131 (2004).
6. H. Chand, R. Srianand, P. Petitjean, B. Aracil, *Astron. Astrophys.* **417**, 853 (2004).
7. M. T. Murphy, J. K. Webb, V. V. Flambaum, *Phys. Rev. Lett.* **99**, 239001 (2007).
8. M. T. Murphy, J. K. Webb, V. V. Flambaum, *Mon. Not. Roy. Astron. Soc.* **384**, 1053 (2008).
9. A. Ivanchik, *et al.*, *Astron. Astrophys.* **440**, 45 (2005).
10. E. Reinhold, *et al.*, *Phys. Rev. Lett.* **96**, 151101 (2006).
11. P. Tzanavaris, M. T. Murphy, J. K. Webb, V. V. Flambaum, S. J. Curran, *Mon. Not. Roy. Astron. Soc.* **374**, 634 (2007).
12. V. V. Flambaum, M. G. Kozlov, *Phys. Rev. Lett.* **98**, 240801 (2007).
13. J. van Veldhoven, *et al.*, *Euro. Phys. J. D* **31**, 337 (2004).
14. C. Henkel, *et al.*, *Astron. Astrophys.* **440**, 893 (2005).

15. T. Wiklind, F. Combes, *Astron. Astrophys.* **299**, 382 (1995).
16. Materials and methods are available as supporting material on *Science Online*.
17. VPFIT is maintained by R. F. Carswell. See <http://www.ast.cam.ac.uk/~rfc/vpfit.html>.
18. J. G. Cohen, C. R. Lawrence, R. D. Blandford, *Astrophys. J.* **583**, 67 (2003).
19. T. York, N. Jackson, I. W. A. Browne, O. Wucknitz, J. E. Skelton, *Mon. Not. Roy. Astron. Soc.* **357**, 124 (2005).
20. A. R. Patnaik, *et al.*, *Mon. Not. Roy. Astron. Soc.* **261**, 435 (1993).
21. Throughout we employ a standard  $\Lambda$  cosmology with  $H_0 = 71 \text{ km s}^{-1} \text{ Mpc}^{-1}$ ,  $\Omega_m = 0.27$  and  $\Omega_\Lambda = 0.73$  whereby  $z = 0.68466$  corresponds to a look-back time of 6.2 Gyr ( $\sim$ half the age of the Universe) with a linear angular scale of  $7.1 \text{ pc mas}^{-1}$ .
22. A. D. Biggs, *et al.*, *Mon. Not. Roy. Astron. Soc.* **338**, 599 (2003).
23. C. L. Carilli, M. P. Rupen, B. Yanny, *Astrophys. J.* **412**, L59 (1993).
24. N. Kanekar, J. N. Chengalur, A. G. de Bruyn, D. Narasimha, *Mon. Not. Roy. Astron. Soc.* **345**, L7 (2003).
25. N. Jethava, C. Henkel, K. M. Menten, C. L. Carilli, M. J. Reid, *Astron. Astrophys.* **472**, 435 (2007).
26. F. Combes, T. Wiklind, *Astrophys. J.* **486**, L79 (1997).
27. K. M. Menten, M. J. Reid, *Astrophys. J.* **465**, L99 (1996).
28. C. L. Carilli, *et al.*, *Phys. Rev. Lett.* **85**, 5511 (2000).
29. S. Muller, M. Guélin, F. Combes, T. Wiklind, *Astron. Astrophys.* **468**, L53 (2007).
30. T. Wiklind, F. Combes, *Highly Redshifted Radio Lines*, C. L. Carilli, S. J. E. Radford, K. M. Menten, G. I. Langston, eds. (Astron. Soc. Pac., San Francisco, CA, U.S.A, 1999), vol. 156 of *ASP Conf. Ser.*, p. 202–209.
31. MTM thanks the Australian Research Council for a QEII Research Fellowship (DP0877998).

### Supporting Online Material

[www.sciencemag.org](http://www.sciencemag.org)

Materials and Methods

Figs. S1 to S3

Tables S1 and S2

References and Notes

11 February 2008; accepted 22 May 2008

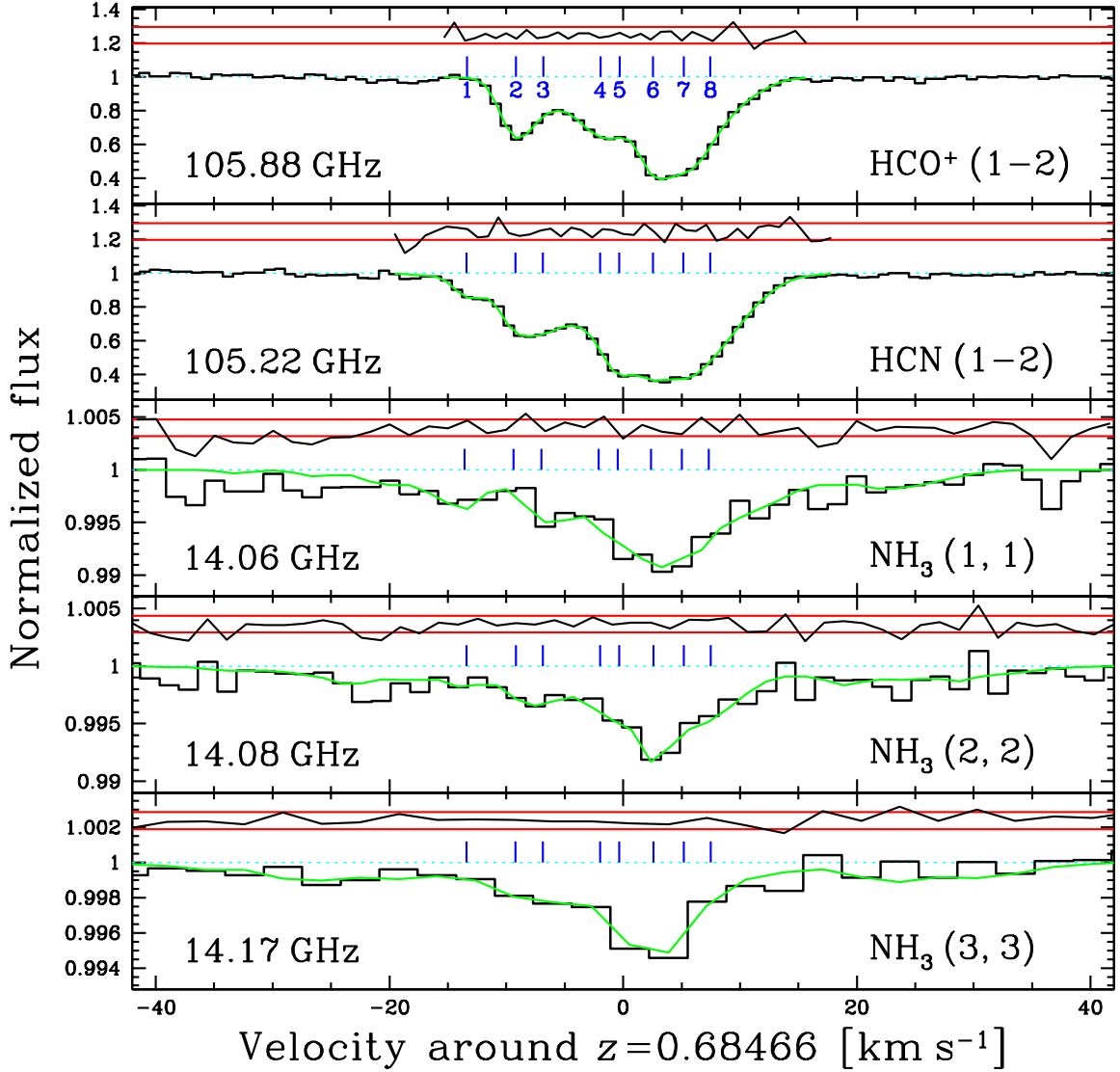


Figure 1: Spectra of the molecular transitions used in this study registered to a heliocentric velocity scale centered on  $z = 0.68466$ . The nominal observed frequencies are noted in each panel. The data, normalized by fits to their continua, are plotted as black histograms. Tick-marks above the spectra show the positions of velocity components in our fiducial 8-component fit (solid line following the data). Note that the HCN and  $\text{NH}_3$  transitions have complex hyperfine structure reflected in each velocity component; the tick marks show the position of the strongest hyperfine component in LTE [see (16)]. Residuals between the fit and data, normalized by the (constant) error array, are plotted above the spectra, bracketed by horizontal lines representing the  $\pm 1 \sigma$  level. The fit contains 57 free parameters: an optical depth for each component in each transition ( $5 \times 8$  parameters) plus a Doppler width and redshift for each component ( $8+8$  parameters) and a single value of  $\Delta\mu/\mu$ . The fitted line parameters are tabulated in (16).

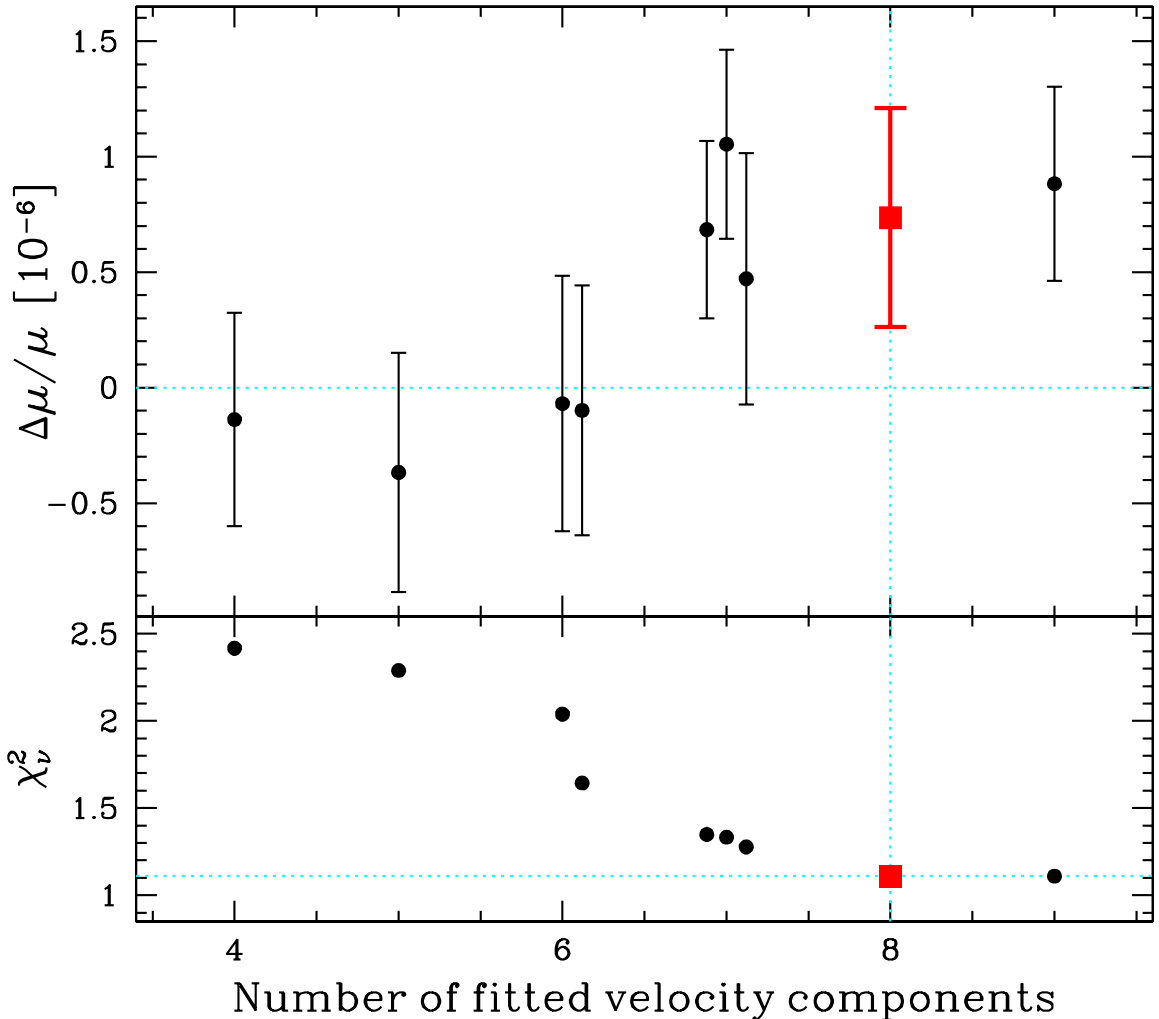


Figure 2: Variation in  $\Delta\mu/\mu$  and  $\chi^2$  per degree of freedom,  $\chi^2_\nu$ , of different velocity structures characterized by the number of fitted absorption components.  $\chi^2_\nu$  is defined as  $\chi^2/\nu \equiv \sum_j^{N_d} [d_j - m(j)]/\sigma_j^2$  for  $d_j$  the  $j^{\text{th}}$  data value with variance  $\sigma_j^2$  and model value  $m(j)$ . The sum is over all  $N_d = 223$  data points;  $\nu \equiv N_d - N_{\text{par}}$  for  $N_{\text{par}}$  free model parameters. Our fiducial 8-component ( $N_{\text{par}} = 57$ ) result is highlighted with square points. Different components were added/removed to/from the fiducial fit to form each initial velocity structure and VPFIT was run again to minimize  $\chi^2$  by varying all free parameters. Two different initial fits with 6 components and three fits with 7 components were possible; the different results are offset in the plot for clarity in these cases. Large  $\chi^2_\nu$  values for  $\leq 6$  components indicate that those fits are not statistically acceptable. Of the remaining fits, the 8-component fit has the lowest  $\chi^2_\nu$ . Note that the 9-component fit has a smaller  $\chi^2$  (because more parameters are being fitted) but a marginally higher  $\chi^2_\nu$ , indicating that it is less statistically preferred than the 8-component fit. Only statistical error bars on  $\Delta\mu/\mu$  are shown; see text for discussion about systematic errors.

# SUPPORTING ONLINE MATERIAL

## Materials and methods

### New observations of $\text{HCO}^+$ and $\text{HCN}(1-2)$

The  $\text{HCO}^+$  and  $\text{HCN}(1-2)$  spectra were obtained with the Plateau de Bure Interferometer (PdBI) with the 3-mm receivers, the  $\text{HCO}^+(1-2)$  line being redshifted to 105.882 GHz and the  $\text{HCN}(1-2)$  line to 105.221 GHz. Five or six antennas were used in compact configurations, and the two images, A and B, of B0218+357 were not resolved from each other. The continuum flux density of B0218+357 was estimated to be  $\sim 0.5$  Jy.

The spectra presented here are averages of spectra taken on several observing runs: 28 and 29 June 2005, 15 July 2006 and 23 March 2007 for the  $\text{HCO}^+$  data; 5 July 2005, 19 August 2006 and 23 March 2007 for the  $\text{HCN}$  data. The integration time varied from 30-min to  $\sim 2$ -hr. Within the SNR of individual integrations, we do not see time variation in the absorption profiles between 2005 and 2007. Note that in March 2007 the  $\text{HCO}^+$  and  $\text{HCN}$  data were obtained simultaneously with dual polarization receivers.

The frequency dependence of the instrument across the spectral bandwidth (80 MHz with 256 channels of width  $\sim 0.3$  MHz) was calibrated by observing a strong radio quasar for several minutes. Its amplitude and phase as a function of radio frequency were solved for by fitting high order polynomials (10 and 20, respectively). The RMS residuals of the bandpass calibration were typically less than 1–2%. The visibilities were self-calibrated with respect to the continuum emission of B0218+357 itself: the phase was referenced to the barycenter of the continuum emission and the amplitude was normalized to the total continuum flux. The spectra observed with the different baselines of the interferometer and at different epochs were then co-added. Third-degree baselines (derived on channels free of absorption) were subtracted from these final spectra to remove small residuals in the radio bandpass calibration, instrument drifts and/or atmospheric fluctuations.

### Laboratory molecular data

Table S1 provides all the laboratory molecular data used in our analysis. Laboratory frequencies for  $\text{HCO}^+$  and  $\text{HCN}(1-2)$  were taken from (S1) and (S2) respectively, as recommended by (S3). Frequencies for the  $\text{NH}_3$  inversion lines were taken from (S4). Including the hyperfine structure of the  $\text{HCN}(1-2)$  and  $\text{NH}_3$  inversion transitions when fitting the absorption spectra is very important. The relative optical depths of the  $\text{HCN}(1-2)$  hyperfine components, assumed to be in LTE, were taken from (S3) while those for the  $\text{NH}_3$  lines were computed using the formula presented by (S4).

## Alternative $\chi^2$ minimization scheme

The simplest, fastest and most robust method of determining  $\Delta\mu/\mu$  from a multi-component, simultaneous fit to different transitions is simply to include  $\Delta\mu/\mu$  as an additional free parameter in the  $\chi^2$  minimization process. This was our approach in the main text. An alternative approach is to conduct many simultaneous fits to the absorption spectra, each with a fixed input value of  $\Delta\mu/\mu$  but allowing all other free parameters to vary, to build up a ‘ $\chi^2$  curve’ – a plot of  $\chi^2$  versus  $\Delta\mu/\mu$ . The best-fitting value of  $\Delta\mu/\mu$  is the one which produces the lowest value of  $\chi^2$ ,  $\chi_{\min}^2$ . The functional form of  $\chi^2$  implies that the  $\chi^2$  curve should be near parabolic and smooth on scales similar to the  $1\text{-}\sigma$  error on  $\Delta\mu/\mu$ . The error can therefore be determined from the width of the  $\chi^2$  curve near the minimum; the curve’s smoothness is obviously essential to this procedure – see (7, 8), cf. (6).

Figure S1 shows the  $\chi^2$  curve for our fiducial 8-component fit to the rotational and  $\text{NH}_3$  inversion spectra. For convenience, we plot  $\Delta\chi^2 \equiv \chi^2 - \chi_{\min}^2$  normalized by the lowest value of  $\chi_{\nu}^2$  – i.e.  $\chi^2$  per degree of freedom – in the curve,  $\chi_{\nu,\min}^2$ . This representation allows the  $1\text{-}\sigma$  error in  $\Delta\mu/\mu$  to be determined directly from the width of the curve at  $\Delta\chi^2/\chi_{\nu,\min}^2 = 1$ . The result from this process is  $\Delta\mu/\mu = (+0.75 \pm 0.45) \times 10^{-6}$ , in very close agreement with the value determined simply by fitting  $\Delta\mu/\mu$  as an additional free parameter,  $\Delta\mu/\mu = (+0.74 \pm 0.47) \times 10^{-6}$ .

## Errors from bandpass calibration and baseline stability?

Possible observational systematic uncertainties include bandpass calibration errors and variable spectral baselines. The former may affect the PdBI (i.e. interferometric) rotational spectra while the latter will be most severe for the single-dish  $\text{NH}_3$  spectra which were obtained with the Effelsberg 100-m Ratio Telescope in Germany. Both these effects could potentially lead to small ripples in the absorption spectra. As mentioned above, the RMS bandpass calibration errors for the new rotational spectra are  $<2\%$ . Additionally, the fact that  $\Delta\mu/\mu$  is insensitive to the rotational transition used in the analysis suggests that any residual ripples in the  $\text{HCO}^+$  or  $\text{HCN}(1\text{--}2)$  spectra are unimportant. The poorer SNR (on the optical depth) of the  $\text{NH}_3$  transitions makes individually removing them a less stringent test. Nevertheless, removing  $\text{NH}_3(1,1)$  yields  $\Delta\mu/\mu = (+0.67 \pm 0.62)$ , removing  $\text{NH}_3(2,2)$  gives  $(+0.65 \pm 0.62)$  and eliminating  $\text{NH}_3(3,3)$  provides  $(+0.84 \pm 0.49)$ , all in units of  $10^{-6}$ . Wald–Wolfowitz runs tests on the unabsorbed portions of the  $\text{NH}_3$  spectra also reveal no evidence for significant ripples. Therefore, there is no evidence for significant systematic effects due to bandpass calibration and/or baseline stability problems.

## Alternative velocity structures

As described in the main text, we fitted several different velocity structures in our search for the one with the lowest  $\chi_{\nu}^2$ , i.e. the fiducial 8-component model plotted in Fig. 1. For each

velocity structure, VPFIT was run again to minimize  $\chi^2$  by varying all free parameters of the fit. These alternative fits provided the black points in Fig. 2. For comparison, Fig. S2 plots these alternative structures in the same way as Fig. 1. By inspecting the residual spectra (plotted above each transition), it is easy to see why the fits with fewer than 8 components result in larger values of  $\chi^2_\nu$  compared to the fiducial model. The residuals take many-pixel excursions outside the  $1\text{-}\sigma$  ranges at similar velocities in different transitions – a sure sign that real structure exists in the absorption profiles which is left unaccounted for by the fit. For example, the human eye readily picks out 5 or 6 components in the rotational profiles but the two different 6-component models produce very poor fits (two right-hand panels in middle row) with  $\chi^2_\nu > 1.6$  in Fig. 2. On the other hand, the 9-component model provides “too good” a fit, as demonstrated by its marginally *higher*  $\chi^2_\nu$  value in Fig. 2 compared to the fiducial model. The best-fit line parameters for the fiducial 8-component model are given in Table S2.

The high SNR of the  $\text{HCO}^+$  and  $\text{HCN}(1\text{--}2)$  spectra implies that our determination of the velocity structure is driven by those transitions and not the  $\text{NH}_3$  inversion lines. A good cross-check on the central assumption in our analysis – that the velocity structure is the same in different transitions – can therefore be made by fitting the  $\text{HCO}^+$  and  $\text{HCN}(1\text{--}2)$  spectra separately. Fig. S3 compares our independent fits of these rotational lines. Only the velocity structures providing the lowest  $\chi^2_\nu$  values are plotted. Seven components provide the lowest- $\chi^2_\nu$  fit for the  $\text{HCO}^+$  data while 8 components are required to fit the  $\text{HCN}$  spectrum. However, as for our fiducial simultaneous fit in Fig. 1, the bluest component in  $\text{HCN}$  is not statistically required by the  $\text{HCO}^+$  data. That is, both the  $\text{HCN}$  and  $\text{HCO}^+$  data can be individually fit by the same number of components as used in the simultaneous fit. Also note the general agreement between the velocities at which these components are best fitted. In this sense the velocity structures of the two high SNR rotational transitions are consistent.

## **Errors from morphology and variability of B0218+357?**

Quasars are not point sources at radio wavelengths but instead show sometimes complex morphological structure. Indeed, each lensed image of B0218+357 shows a core–jet morphology. If the absorbing molecular clouds at  $z = 0.68466$  have smaller angular extent than the background radio source, and the source’s morphology varies between 24 and 178 GHz (in the absorber’s reference frame), then the  $\text{NH}_3$  and rotational transitions may arise along slightly different sight-lines. This may, in principle, lead to systematic errors in the determination of  $\Delta\mu/\mu$ .

As discussed in the main text, all the molecular absorption lines studied here are very likely to arise only towards the core of image A. Its angular extent,  $<1 \times 1$  mas, places an upper limit on the spatial extent of the absorbing region of just  $<7 \times 7$  pc (14, 29, 21). This is a typical size for Galactic molecular clouds (S5). Nevertheless, if the core is close to the upper limit in angular extent and/or if the absorbing clouds are smaller than  $\sim 5$  pc, then it is possible that the  $\text{NH}_3$  and rotational profiles may have different velocity structures. The similarity of the velocity structures of a variety of transitions – covering a larger frequency range than just those studied

here – suggests this may be of little concern.

However, evidence for small-scale structure of the absorbing clouds has been found in (30). By examining the optical obscuration and reddening of image A by dust expected to reside in the absorbing clouds, (30) established that not all of image A’s optical emission is obscured and that its unobscured portion is not even substantially reddened. Therefore, assuming that the main component of optical emission originates from image A’s core (just as for the radio emission), the absorbing clouds must not completely cover the background emission. Since the emission region’s size should vary with frequency, the NH<sub>3</sub> profiles may contain a different number of absorbing velocity components compared to the rotational profiles (though some components may still be in common).

The flux variability of B0218+357 may also be of potential concern. Again, if the absorbing clouds do not cover the core of image A and its morphology changes with time, then observations at different epochs may probe slightly different sight-lines. As detailed above, the HCO<sup>+</sup> and HCN(1–2) data were obtained over several runs between June 2005 and March 2007 with HCO<sup>+</sup> usually observed up to 1 month before HCN. The NH<sub>3</sub> data were collected in August 2001 and June 2002.

It is difficult to use the available data to test specifically for each of these effects. Nevertheless, the fact that the low SNR NH<sub>3</sub> profiles at least resemble the higher SNR rotational ones – particularly the velocity of the peak optical depth – allows a general quantitative assessment of the likely effect on the  $\Delta\mu/\mu$  measurement. One test is to remove specific (groups of) velocity components from the fits to the NH<sub>3</sub> spectra while keeping the fiducial 8-component model for the rotational lines. Upon removing a single velocity component – that is, fitting 7 components to the NH<sub>3</sub> spectra – the different possible fits yield an RMS deviation of  $0.5 \times 10^{-6}$  from our fiducial  $\Delta\mu/\mu$ . This is dominated by the results of removing either component 3 or component 6 (see Fig. 1), which give deviations of  $\approx 0.7 \times 10^{-6}$ . Removing selected pairs of components (e.g. 1 & 3 or 5 & 7 etc.) or selected combinations of three components yield similar RMS deviations of  $\approx 0.5 \times 10^{-6}$ ; these are again dominated by cases where either components 3 or 6 are removed. Another test is to fit the NH<sub>3</sub> profiles with as few components as is statistically acceptable (i.e.  $\chi^2_\nu \sim 1$ ) – in our case just two, components 3 & 6 – while keeping the full velocity structure in the rotational lines. For this test we relaxed the constraint that the widths of the rotational and NH<sub>3</sub> components should be the same. We find a deviation of  $0.45 \times 10^{-6}$  from the fiducial value to  $\Delta\mu/\mu = (+0.29 \pm 0.39) \times 10^{-6}$ .

Given these results, we adopt a representative systematic error on  $\Delta\mu/\mu$  of  $\pm 0.7 \times 10^{-6}$  due to possible differences in the velocity structure of the rotational and NH<sub>3</sub> spectra. Note that if higher resolution, higher SNR NH<sub>3</sub> spectra were obtained, a more direct comparison of the NH<sub>3</sub> velocity structure with that of the rotational transitions could be made, similar to the comparison of the two rotational transitions made above. Therefore, high quality NH<sub>3</sub> spectra should reduce the systematic error calculated here.

## Optical depths

Neither the PdBI rotational observations nor the Effelsberg  $\text{NH}_3$  observations resolved the two lensed images from each other. Thus, even though the molecular absorption is very likely to arise only towards the core of image A, continuum flux from image B, the jet of image A and possibly the Einstein ring will also contribute to the spectra studied here. The flat-spectrum lensed cores of images A and B are thought to dominate the continuum flux beyond 14 GHz and image A contributes  $>70\%$  of the flux (*S6, 14, 29*). Therefore, the fraction of image A’s core continuum absorbed by the  $\text{NH}_3$  and rotational lines is about a factor of 1.4 larger than shown in Fig. 1. Thus, if some velocity components truly absorb all of image A’s core continuum (at the observed spectral resolution), they will appear flat-bottomed but will not extend down to the zero flux level.

For simplicity, we did not attempt to take this potential effect into account in the profile fits in Fig. 1. It is clearly not a problem for the  $\text{NH}_3$  inversion lines since they only absorb  $\sim 1\%$  of the total continuum flux. However, it is possible that some velocity components in  $\text{HCO}^+$  and  $\text{HCN}(1-2)$  are near saturation (see below), even though we do not observe flat-bottomed profiles. We tested the effect of this scenario on  $\Delta\mu/\mu$  in the following way: 30% of the flux was subtracted from the rotational spectra and the continuum levels were appropriately renormalized. Instead of Gaussian absorption components we fitted Voigt profiles to allow saturation effects in the fit. We conducted several fits with a range of quantum mechanical damping coefficients to characterize the onset of damping wings in the Voigt profiles. All fits gave results negligibly different to our fiducial result, indicating that, under the assumption that our fitted velocity structure reflects the real velocity distribution of absorbing clouds, saturation effects do not affect our measurement of  $\Delta\mu/\mu$ .

It is likely that some of the stronger components in the  $\text{HCO}^+$  and  $\text{HCN}(1-2)$  profiles are optically thick. Precise optical depths are difficult to determine because the fraction of the background source covered by the absorption clouds is also unknown. Wiklind & Combes (*15*) found optical depths of  $\gtrsim 1.9$  for  $\text{HCN}(1-2)$  and  $\gtrsim 1.1$  for  $\text{HCO}^+(1-2)$ . A similar conclusion was reached for  $\text{HCO}^+(1-2)$  by (*29*). If several velocity components with very similar velocities ( $\Delta v \lesssim 2 \text{ km s}^{-1}$ ) and different optical depths exist in the rotational spectra but are fitted as a single component, then some spurious shifts with respect to the optically thin  $\text{NH}_3$  profile might be measured. The potential systematic error on  $\Delta\mu/\mu$  is therefore the same as that caused by uncertainty in the  $\text{NH}_3$  velocity structure, as quantified above.

## Errors from hyperfine structure?

All the fits discussed in the main text and above assumed that the relative optical depths of the  $\text{HCN}(1-2)$  and  $\text{NH}_3$  hyperfine structure components were those expected in LTE – see Table S1. However, non-LTE hyperfine structure effects have been observed in  $\text{HCN}(0-1)$  emission lines from Galactic interstellar clouds (*S7*). Nevertheless, if LTE conditions do not prevail for the  $\text{HCN}(1-2)$  velocity components, then the effect on  $\Delta\mu/\mu$  seems to be small since remov-

ing HCN(1–2) from the analysis does not change our measured  $\Delta\mu/\mu$  substantially (see main text). However, removing the NH<sub>3</sub> transitions is not possible if we are still to measure  $\Delta\mu/\mu$ , nor are the NH<sub>3</sub> spectra of high enough quality to directly determine the hyperfine structure populations; the potential effect of non-LTE hyperfine structure must be assessed differently.

NH<sub>3</sub> hyperfine structure ‘anomalies’ have previously been found in Galactic sources both in absorption (*S8*) and emission (*S9*). The non-LTE conditions cause the  $\Delta F_1 \neq 0$  ‘satellite’ components with a given quadrupole quantum number,  $F_1$ , to have different optical depth depending on the change in  $F_1$  during the transition. Since complementary (i.e.  $F_1=1-2$  and  $F_1=2-1$ ) transitions straddle the main ( $\Delta F_1 = 0$ ) hyperfine components, non-LTE conditions cause asymmetries in the optical depth profile of any given velocity component. A simple test to gauge the maximum effect this may have on  $\Delta\mu/\mu$  is to remove either the high or low frequency satellite lines from the NH<sub>3</sub> fits. This causes RMS deviations from our fiducial  $\Delta\mu/\mu$  of  $0.3 \times 10^{-6}$ . We adopt this as a second component to our systematic error budget in the main text. Note that with higher resolution, higher SNR NH<sub>3</sub> spectra it should be possible to conduct consistency checks for strong non-LTE hyperfine structure effects, thereby reducing the possible systematic error.

## Reference frames

All the spectra studied here were shifted to the heliocentric rest frame so that any velocity shifts between them could be attributed to a varying  $\mu$ .

Depending on the format in which raw radio telescope data are recorded, passed to the data reduction software and processed, one or more small velocity shifts may be applied to them. These typically convert between the local standard of rest (LSR) and heliocentric frames. However, the Doppler correction for the radial velocity,

$$\frac{v_{\text{rad}}}{c} = \frac{\nu_{\text{obs}}^2 - \nu_0^2}{\nu_{\text{obs}}^2 + \nu_0^2}, \quad (2)$$

is approximated in many data reduction software packages (for traditional reasons, not ones of simplicity or processing speed etc.) by

$$\frac{v_{\text{rad}}}{c} \approx \frac{\nu_{\text{obs}} - \nu_0}{\nu_0} \quad (3)$$

which applies when  $v_{\text{rad}}/c \ll 1$ . Here  $\nu_0$  is the emitted frequency and  $\nu_{\text{obs}}$  is the observed frequency. Since we are interested in small shifts between different transitions with a precision of  $\delta(\Delta\mu/\mu) \sim 0.1 \times 10^{-6}$ , corresponding to a velocity shift of just  $0.1 \text{ km s}^{-1}$ , we must check whether the above approximation is accurate enough so as not to cause systematic errors in  $\Delta\mu/\mu$ . The difference between the above two expressions for the Doppler correction is approximately  $(v_{\text{rad}}/c)^2$  for  $v_{\text{rad}}/c \ll 1$ . So, for a maximal heliocentric correction of  $\sim 30 \text{ km s}^{-1}$ , the systematic error introduced by using the approximation is  $\sim 3 \text{ m s}^{-1}$ . This corresponds to  $\delta(\Delta\mu/\mu) \sim 3 \times 10^{-9}$ , well below our current statistical precision.

## References and Notes

- S1. F. De Lucia, W. Gordy, *Phys. Rev.* **187**, 58 (1969).
- S2. K. V. L. N. Sastry, E. Herbst, F. C. De Lucia, *J. Chem. Phys.* **75**, 4169 (1981).
- S3. H. M. Pickett, *et al.*, *J. Quant. Spectrosc. Radiat. Transfer* **60**, 883 (1998).
- S4. S. G. Kukolich, *Phys. Rev.* **156**, 83 (1967).
- S5. S. Terebey, M. Fich, L. Blitz, C. Henkel, *Astrophys. J.* **308**, 357 (1986).
- S6. A. R. Patnaik, R. W. Porcas, I. W. A. Browne, *Mon. Not. Roy. Astron. Soc.* **274**, L5 (1995).
- S7. J. Cernicharo, A. Castets, G. Duvert, S. Guilloteau, *Astron. Astrophys.* **139**, L13 (1984)
- S8. D. N. Matsakis, *et al.*, *Astrophys. J.* **214**, L67 (1977).
- S9. J. Stutzki, M. Olberg, G. Winnewisser, J. M. Jackson, A. H. Barrett, *Astron. Astrophys.* **139**, 258 (1984).

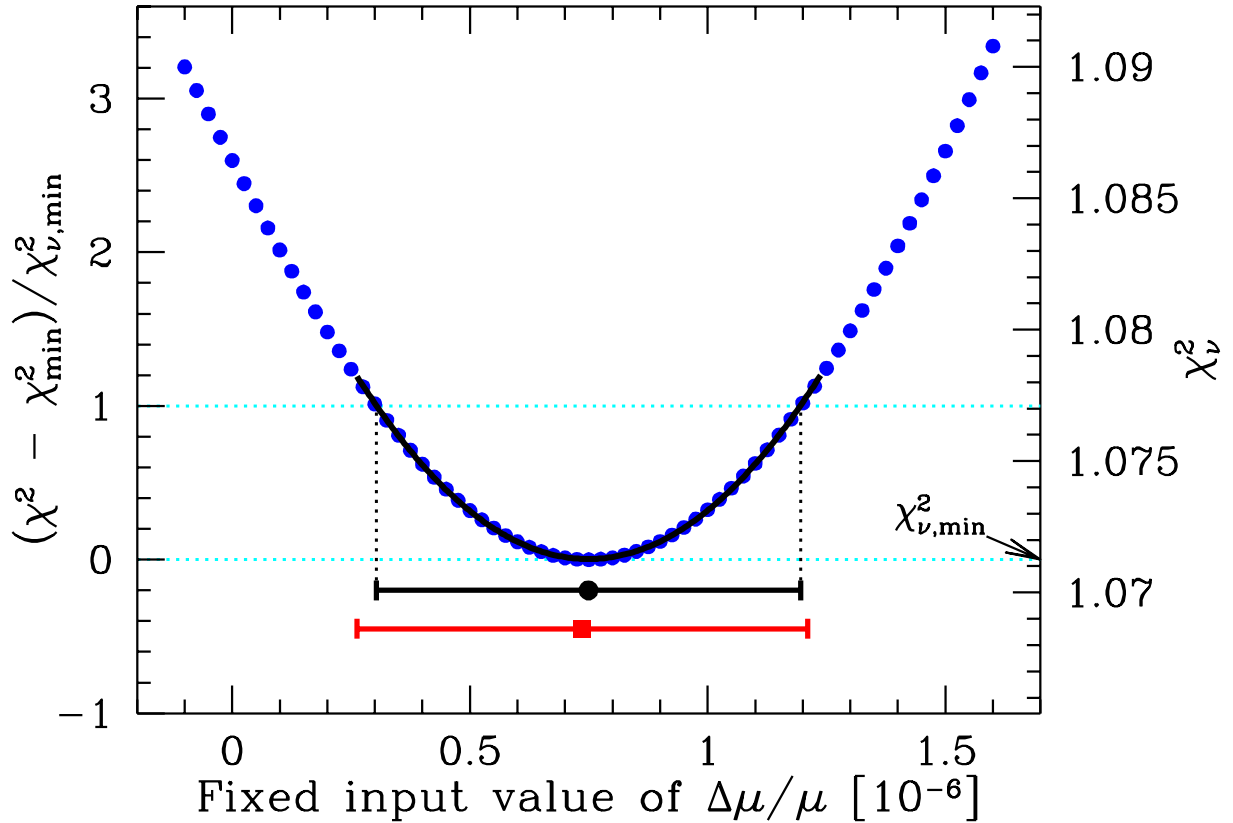


Figure S1:  $\chi^2$  curve for the fiducial 8-component model fit. Note its (required) smoothness and (expected) near-parabolic shape. The right-hand vertical scale shows  $\chi^2_\nu$  which takes a minimum value of  $\chi^2_{\nu,\min} = 1.07125$ . The left-hand vertical scale shows  $\Delta\chi^2/\chi^2_{\nu,\min}$ , thereby allowing the  $1\text{-}\sigma$  error in  $\Delta\mu/\mu$  to be immediately read off the graph (dotted black lines). In practice, we measured the position at which  $\chi^2$  takes its minimum and the curve's width by fitting a parabola to the central points; the fit, marked by the black solid line, demonstrates how close to parabolic that part of the curve is. The black circle and error-bar represent the result from this fit,  $\Delta\mu/\mu = (+0.75 \pm 0.45) \times 10^{-6}$ , which closely matches our fiducial value represented by the red/grey square and error-bar.

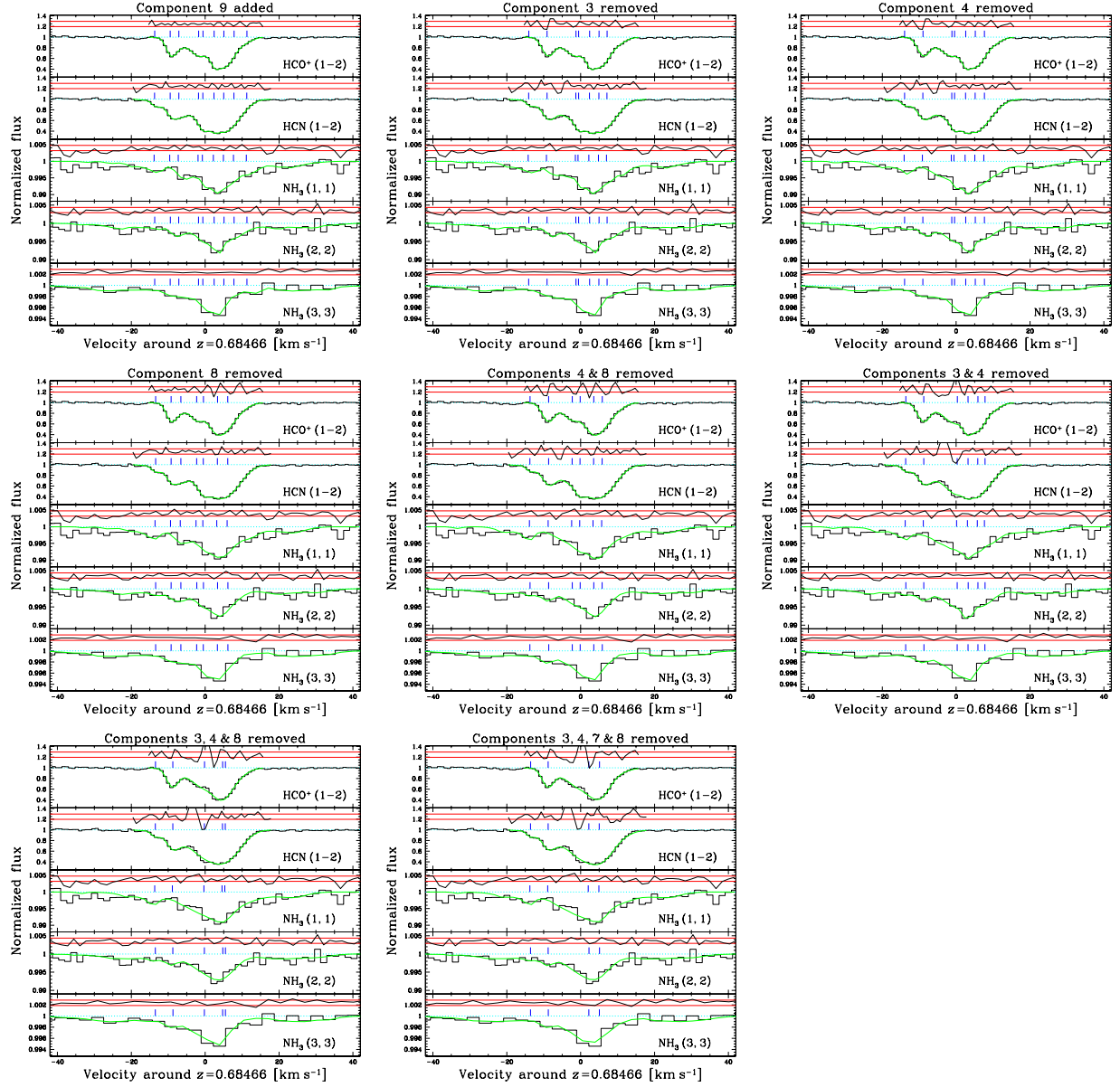


Figure S2: The different velocity structures attempted in search of the statistically preferred one. The values of  $\Delta\mu/\mu$  and  $\chi^2_\nu$  corresponding to each fit are represented by the black points in Fig. 2. Components were removed/added from/to the fiducial fit to form each initial velocity structure and VPFIT was run again to minimize  $\chi^2$ . For the 9-component model, the additional component was added redwards of all other components. The residual spectra show how poor the fits are with  $\leq 6$  components.

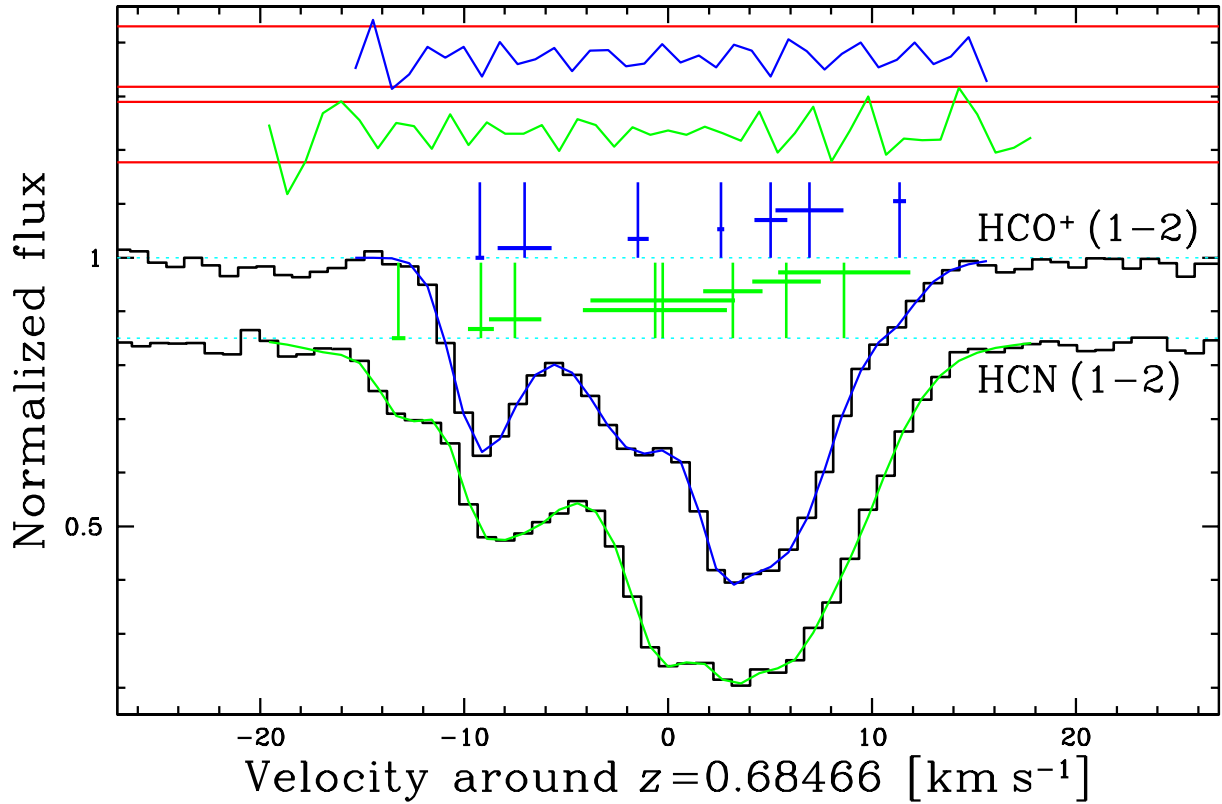


Figure S3: Independent fits to the two rotational transitions studied here. Layout similar to Fig. 1. The data, tick-marks and residuals for HCN(1–2), marked in lighter grey lines, are offset below those for HCO<sup>+</sup> for clarity. The formal 1- $\sigma$  statistical error in the redshift of each component (converted to velocity) is represented by the horizontal bars across the tick marks. The error bar for each component is plotted higher than the one to its left for clarity. There is broad agreement between the positions of the velocity components. The bluest component in HCN(1–2) is not statistically required by the HCO<sup>+</sup>(1–2) data alone, similar to the simultaneous fit in Fig. 1.

Table S1: Laboratory frequencies of transitions used in our analysis. The second and third columns provide, respectively, the relevant quantum numbers for the lower and upper states in the following order:  $J, F, F_1$ . For  $\text{HCO}^+(1-2)$  only  $J$  is relevant while  $F_1$  is not relevant for  $\text{HCN}(1-2)$ . For the  $\text{NH}_3$  inversion transitions,  $J = K$ ,  $F$  is the magnetic hyperfine quantum number and  $F_1$  is the quadrupole quantum number. The final column shows the relative optical depth of different hyperfine components,  $\Sigma$ , in LTE.  $\Sigma$  is normalized to unity for the strongest hyperfine component.

Molecule	Transition		Frequency [GHz]	log $\Sigma$
	Lower	Upper		
$\text{HCO}^+$	1	2	178.375065(50)	0.0000
$\text{HCN}$	1, 2	2, 2	177.2596770(20)	-0.7482
$\text{HCN}$	1, 0	2, 1	177.2599230(20)	-0.6233
$\text{HCN}$	1, 1	2, 2	177.2611100(20)	-0.2711
$\text{HCN}$	1, 2	2, 3	177.2612230(20)	0.0000
$\text{HCN}$	1, 2	2, 1	177.2620122(11)	-1.9243
$\text{HCN}$	1, 1	2, 1	177.2634450(20)	-0.7482
$\text{NH}_3$	1, 1/2, 1	1, 1/2, 0	23.692926829(56)	-0.7993
$\text{NH}_3$	1, 3/2, 1	1, 1/2, 0	23.692968829(38)	-0.4983
$\text{NH}_3$	1, 1/2, 1	1, 3/2, 2	23.693872152(57)	-0.7024
$\text{NH}_3$	1, 3/2, 1	1, 5/2, 2	23.693905112(58)	-0.4472
$\text{NH}_3$	1, 3/2, 1	1, 3/2, 2	23.693914466(39)	-1.4014
$\text{NH}_3$	1, 1/2, 1	1, 1/2, 1	23.694459098(36)	-1.1004
$\text{NH}_3$	1, 1/2, 1	1, 3/2, 1	23.694470034(28)	-1.4014
$\text{NH}_3$	1, 3/2, 2	1, 5/2, 2	23.694470904(63)	-1.1461
$\text{NH}_3$	1, 3/2, 2	1, 3/2, 2	23.694480291(44)	-0.1919
$\text{NH}_3$	1, 3/2, 1	1, 1/2, 1	23.694501428(59)	-1.4014
$\text{NH}_3$	1, 5/2, 2	1, 5/2, 2	23.694505950(37)	0.0000
$\text{NH}_3$	1, 3/2, 1	1, 3/2, 1	23.694512322(37)	-0.7024
$\text{NH}_3$	1, 5/2, 2	1, 3/2, 2	23.694515319(47)	-1.1461
$\text{NH}_3$	1, 3/2, 2	1, 1/2, 1	23.695067195(46)	-0.7024
$\text{NH}_3$	1, 3/2, 2	1, 3/2, 1	23.695078206(59)	-1.4014
$\text{NH}_3$	1, 5/2, 2	1, 3/2, 1	23.695113176(50)	-0.4472
$\text{NH}_3$	1, 1/2, 0	1, 1/2, 1	23.696029719(48)	-0.7993
$\text{NH}_3$	1, 1/2, 0	1, 3/2, 1	23.696040646(38)	-0.4983
$\text{NH}_3$	2, 3/2, 2	2, 3/2, 1	23.720534302(33)	-1.7058
$\text{NH}_3$	2, 5/2, 2	2, 3/2, 1	23.720575068(39)	-0.7516
$\text{NH}_3$	2, 3/2, 2	2, 1/2, 1	23.720579876(34)	-1.0068
$\text{NH}_3$	2, 5/2, 2	2, 7/2, 3	23.721336248(58)	-0.7570
$\text{NH}_3$	2, 3/2, 2	2, 5/2, 3	23.721337256(57)	-0.9119
$\text{NH}_3$	2, 5/2, 2	2, 5/2, 3	23.721377951(106)	-2.0580
$\text{NH}_3$	2, 1/2, 1	2, 3/2, 1	23.722588837(70)	-1.0068

Table S1: *continued*

Molecule	Transition		Frequency [GHz]	log $\Sigma$
	Lower	Upper		
NH <sub>3</sub>	2, 3/2, 2	2, 5/2, 2	23.722591529(106)	-1.2621
NH <sub>3</sub>	2, 5/2, 3	2, 7/2, 3	23.722591879(86)	-1.3010
NH <sub>3</sub>	2, 3/2, 2	2, 3/2, 2	23.722632304(33)	-0.3079
NH <sub>3</sub>	2, 5/2, 3	2, 5/2, 3	23.722633644(33)	0.0000
NH <sub>3</sub>	2, 1/2, 1	2, 1/2, 1	23.722634389(33)	-0.7058
NH <sub>3</sub>	2, 5/2, 2	2, 3/2, 2	23.722673071(32)	-1.2621
NH <sub>3</sub>	2, 7/2, 3	2, 5/2, 3	23.722675390(42)	-1.3010
NH <sub>3</sub>	2, 3/2, 1	2, 1/2, 1	23.722679956(22)	-1.0068
NH <sub>3</sub>	2, 5/2, 3	2, 5/2, 2	23.723887894(125)	-2.0580
NH <sub>3</sub>	2, 5/2, 3	2, 3/2, 2	23.723928698(64)	-0.9119
NH <sub>3</sub>	2, 7/2, 3	2, 5/2, 2	23.723929630(50)	-0.7570
NH <sub>3</sub>	2, 1/2, 1	2, 3/2, 2	23.724686811(63)	-1.0068
NH <sub>3</sub>	2, 3/2, 1	2, 5/2, 2	23.724691591(57)	-0.7516
NH <sub>3</sub>	2, 3/2, 1	2, 3/2, 2	23.724732357(123)	-1.7058
NH <sub>3</sub>	3, 9/2, 3	3, 7/2, 2	23.867805094(22)	-0.8013
NH <sub>3</sub>	3, 7/2, 3	3, 5/2, 2	23.867816691(45)	-0.9651
NH <sub>3</sub>	3, 3/2, 3	3, 1/2, 2	23.867824516(112)	-1.3541
NH <sub>3</sub>	3, 5/2, 3	3, 3/2, 2	23.867826808(20)	-1.1500
NH <sub>3</sub>	3, 5/2, 3	3, 7/2, 4	23.868438244(47)	-1.0669
NH <sub>3</sub>	3, 7/2, 3	3, 9/2, 4	23.868440344(24)	-0.9428
NH <sub>3</sub>	3, 3/2, 3	3, 5/2, 4	23.868446261(71)	-1.1938
NH <sub>3</sub>	3, 9/2, 3	3, 11/2, 4	23.868450126(71)	-0.8258
NH <sub>3</sub>	3, 3/2, 2	3, 5/2, 2	23.870049079(21)	-0.6059
NH <sub>3</sub>	3, 3/2, 3	3, 5/2, 3	23.870064875(46)	-0.8734
NH <sub>3</sub>	3, 7/2, 3	3, 9/2, 3	23.870067403(53)	-0.8557
NH <sub>3</sub>	3, 9/2, 4	3, 11/2, 4	23.870079000(37)	-0.9130
NH <sub>3</sub>	3, 3/2, 3	3, 3/2, 3	23.870127881(20)	-0.2713
NH <sub>3</sub>	3, 5/2, 4	3, 5/2, 4	23.870129616(20)	0.0000
NH <sub>3</sub>	3, 1/2, 2	3, 1/2, 2	23.870130224(20)	-0.7521
NH <sub>3</sub>	3, 11/2, 4	3, 9/2, 4	23.870180310(69)	-0.9130
NH <sub>3</sub>	3, 9/2, 3	3, 7/2, 3	23.870188326(66)	-0.8557
NH <sub>3</sub>	3, 5/2, 2	3, 3/2, 2	23.870211423(62)	-0.6059
NH <sub>3</sub>	3, 11/2, 4	3, 9/2, 3	23.871807418(23)	-0.8258
NH <sub>3</sub>	3, 5/2, 4	3, 3/2, 3	23.871811331(20)	-1.1938
NH <sub>3</sub>	3, 9/2, 4	3, 7/2, 3	23.871817154(22)	-0.9428
NH <sub>3</sub>	3, 7/2, 4	3, 5/2, 3	23.871819253(22)	-1.0669
NH <sub>3</sub>	3, 3/2, 2	3, 5/2, 3	23.872431263(30)	-1.1500
NH <sub>3</sub>	3, 1/2, 2	3, 3/2, 3	23.872433410(22)	-1.3541
NH <sub>3</sub>	3, 5/2, 2	3, 7/2, 3	23.872441474(22)	-0.9651
NH <sub>3</sub>	3, 7/2, 2	3, 9/2, 3	23.872452975(39)	-0.8013

Table S2: Absorption line parameters and  $1-\sigma$  uncertainties for the 8-component fiducial fit in Fig. 1. The optical depths,  $\tau$ , for the HCN and  $\text{NH}_3$  transitions are summed over all hyperfine components. For  $\text{NH}_3$ ,  $\tau$  is given in units of 0.01.

Com- ponent	Redshift	FWHM [ $\text{km s}^{-1}$ ]	$\tau$			$\tau/10^{-2}$		
			$\text{HCO}^+(1-2)$	HCN(1-2)	$\text{NH}_3(1,1)$	$\text{NH}_3(2,2)$	$\text{NH}_3(3,3)$	
1	0.6845833(12)	$2.80 \pm 0.40$	$0.004^{+0.011}_{-0.003}$	$0.152^{+0.016}_{-0.014}$	$0.31^{+0.25}_{-0.14}$	$0.07^{+0.50}_{-0.06}$	$0.19^{+0.28}_{-0.10}$	
2	0.6846071(12)	$3.00 \pm 0.20$	$0.41^{+0.12}_{-0.10}$	$0.45^{+0.24}_{-0.16}$	$0.00^{+1.3}_{-1.1}$	$0.37^{+0.42}_{-0.20}$	$0.36^{+0.42}_{-0.20}$	
3	0.6846205(34)	$3.56 \pm 1.07$	$0.15^{+0.11}_{-0.06}$	$0.31^{+0.16}_{-0.11}$	$0.61^{+0.28}_{-0.19}$	$0.32^{+0.31}_{-0.16}$	$0.23^{+0.32}_{-0.13}$	
4	0.6846473(133)	$5.11 \pm 2.53$	$0.39^{+0.68}_{-0.25}$	$0.33^{+0.58}_{-0.21}$	$0.44^{+0.91}_{-0.30}$	$0.57^{+1.12}_{-0.38}$	$0.40^{+0.89}_{-0.28}$	
5	0.6846568(9)	$3.14 \pm 0.37$	$0.11^{+0.99}_{-0.10}$	$0.74^{+0.46}_{-0.28}$	$0.84^{+0.71}_{-0.38}$	$0.37^{+7.10}_{-0.35}$	$0.37^{+2.74}_{-0.32}$	
6	0.6846730(19)	$2.86 \pm 0.98$	$0.59^{+1.18}_{-0.40}$	$0.60^{+1.10}_{-0.39}$	$1.26^{+1.30}_{-0.64}$	$1.14^{+1.50}_{-0.65}$	$0.85^{+1.08}_{-0.48}$	
7	0.6846879(38)	$4.25 \pm 1.27$	$0.63^{+0.91}_{-0.37}$	$0.72^{+1.38}_{-0.47}$	$0.86^{+2.00}_{-0.60}$	$0.32^{+4.78}_{-0.30}$	$0.18^{+5.80}_{-0.18}$	
8	0.6847024(138)	$6.55 \pm 2.01$	$0.25^{+0.42}_{-0.16}$	$0.40^{+0.62}_{-0.24}$	$0.43^{+0.87}_{-0.29}$	$0.46^{+0.70}_{-0.28}$	$0.20^{+0.44}_{-0.14}$	